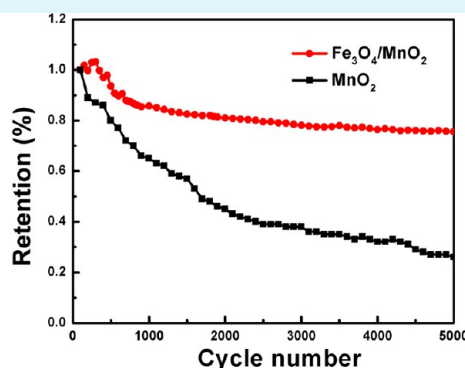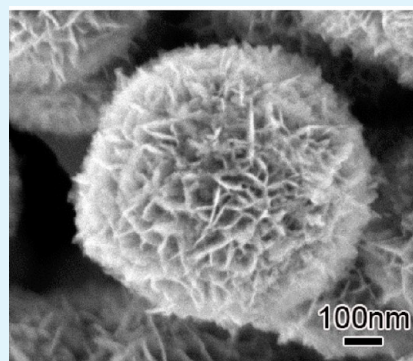# Hierarchically Porous MnO$_2$ Microspheres Doped with Homogeneously Distributed Fe$_3$O$_4$ Nanoparticles for Supercapacitors

Jian Zhu,[‡] Shaochun Tang,*[,‡] Hao Xie, Yuming Dai, and Xiangkang Meng*

National Laboratory of Solid State Microstructures, College of Engineering and Applied Sciences and Institute of Materials Engineering, Nanjing University, Nanjing, Jiangsu 210093, People's Republic of China

S *Supporting Information*

ABSTRACT: Hierarchically porous yet densely packed MnO$_2$ microspheres doped with Fe$_3$O$_4$ nanoparticles are synthesized via a one-step and low-cost ultrasound assisted method. The scalable synthesis is based on Fe^{2+} and ultrasound assisted nucleation and growth at a constant temperature in a range of 25−70 °C. Single-crystalline Fe$_3$O$_4$ particles of 3−5 nm in diameter are homogeneously distributed throughout the spheres and none are on the surface. A systematic optimization of reaction parameters results in isolated, porous, and uniform Fe$_3$O$_4$−MnO$_2$ composite spheres. The spheres' average diameter is dependent on the temperature, and thus is controllable in a range of 0.7−1.28 μm. The involved growth mechanism is discussed. The specific capacitance is optimized at an Fe/Mn atomic ratio of $r = 0.075$ to be 448 F/g at a scan rate of 5 mV/s, which is nearly 1.5 times that of the extremely high reported value for MnO$_2$ nanostructures (309 F/g). Especially, such a structure allows significantly improved stability at high charging rates. The composite has a capacitance of 367.4 F/g at a high scan rate of 100 mV/s, which is 82% of that at 5 mV/s. Also, it has an excellent cycling performance with a capacitance retention of 76% after 5000 charge/discharge cycles at 5 A/g.

KEYWORDS: *manganese dioxide, composite materials, hierarchically porous structures, supercapacitors*

1. INTRODUCTION

Electrochemical capacitors (ECs) are attractive for energy storage because of their fast charging capability and long life. Efficient and low-cost electrode materials are key ingredients necessary for the development of ECs.[1−3] Among the electrode materials available, manganese dioxide (MnO$_2$) is one of the most promising materials because of its high theoretical specific capacitance (∼1370 F/g), low-cost, and environmental benignity. MnO$_2$ nanostructures with regular shapes such as nanowires, -rods, and -sheets show better electrochemical performances than those with irregular shapes.[4−6] Hierarchical MnO$_2$ architectures involving such nanostructures are more likely to have stable specific capacitance (SC) because the whole microsized architecture fixes the nanoporous structure.[7] However, the SC value is still usually much lower with rapid charging/charging and becomes unstable over time.

Porous yet densely packed electrode materials with a high ion-accessible surface area are crucial to the realization of highly stable, high-density electrochemical capacitive energy storage.[8]

In addition, a combination of other materials with MnO$_2$ can further improve electrochemical performances.[9−11] In recent years, extensive research has been focused on nanostructured MnO$_2$-based composites. A choice of newly added metal oxides is determined by whether it improves the performance of capacitance material or not. Copper oxide,[12] ferric oxides,[13] silver oxide,[14] and tin oxide[15,16] have been demonstrated to improve the SC of MnO$_2$. Magnetite (Fe$_3$O$_4$) is a promising electrode material for supercapacitors due to its excellent electrochemical properties,[17−19] but little work has focused on composite capacitance materials combining Fe$_3$O$_4$ with other transition metal oxides. So far, the reported composite electrode materials are mostly core−shell structures.[20,21] Once the shell becomes thick, it exhibits a dense microstructure, which is not beneficial because only the surface area
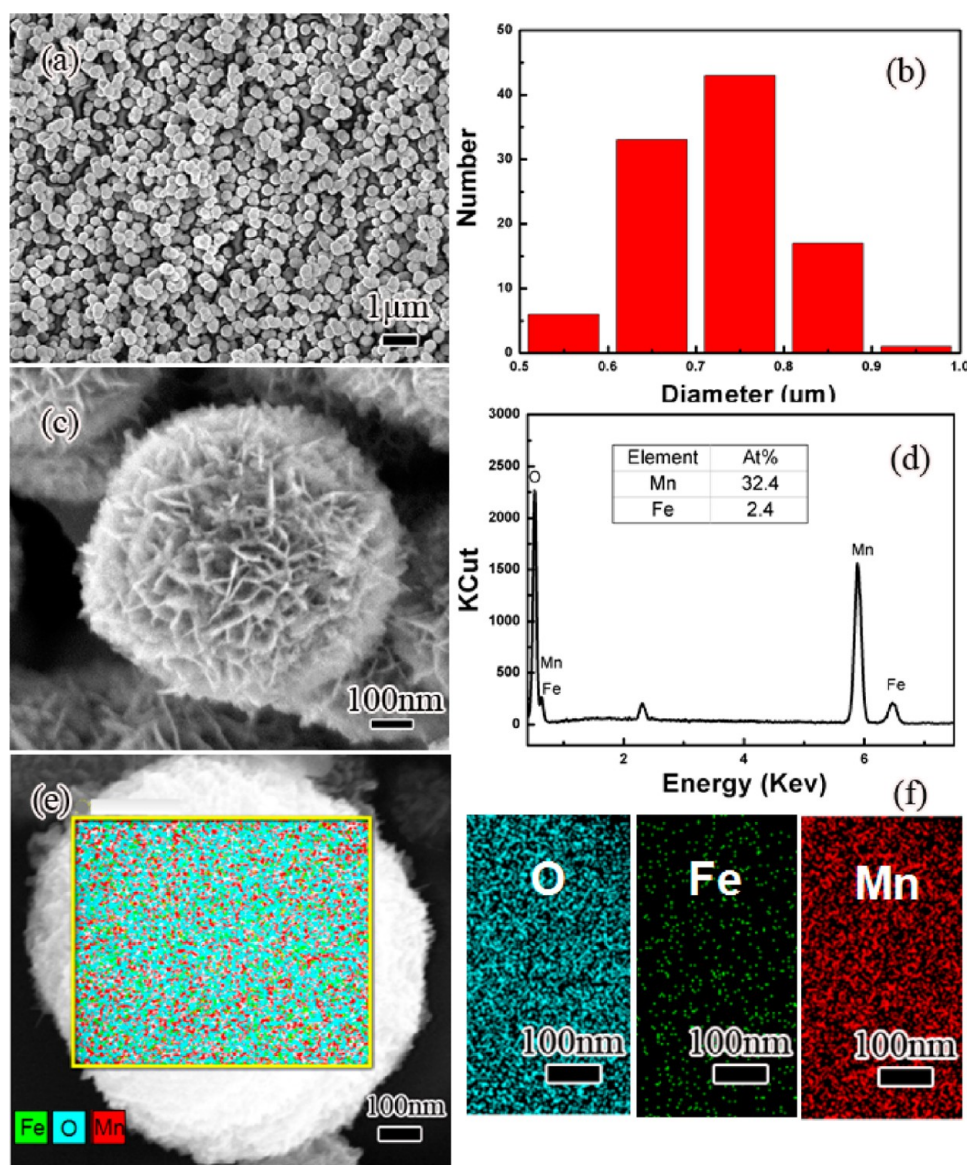
Figure 1. (a) Low- and (c) high-magnification SEM images of the products obtained from a typical synthesis, (b) histograms of diameters for 100 spherical particles. (d) EDS pattern, (e) SEM image with an X-ray elemental mapping recorded from the selected frame on one $Fe_3O_4-MnO_2$ composite particle, and (f) corresponding elemental mappings of different elements.

is involved in charge storage. On the contrary, increasing the SC is difficult as the loading of metal oxides becomes too low. Therefore, hierarchical porous yet densely packed composites with rationally designed compositions and structures are highly desirable. This is because their porosity provides not only a high specific surface area but also a fast ion transport, and they can take full advantages of different components (synergistic effect) to achieve superior electrochemical properties. Due to the synergy, their properties are distinctly different from those of individual metal oxides or their random aggregates. Putting nanoparticles of additional metal oxide into the interior of the MnO_2 matrixes is expected to create compounds with a high and stable SC.

Ultrasound irradiation is powerful for the formation of porous nanostructures. Besides breaking up of larger aggregation, the crucial influence of the ultrasound method also contains improving the transport of crystallites in the solution, generating denser micrometer spheres rather than allowing the growth of flakes first.[22−24] Inspired by this, various

spherical porous nanostructures with improved properties have been achieved by ultrasound assisted synthesis.[25,26] Fe_3O_4 nanoparticles synthesized by this method exhibit remarkable pseudocapacitive activities including high specific capacitance, good rate capability, and excellent cycling stability. Here, we report one-step synthesis of Fe_3O_4-doped MnO_2 microspheres with a hierarchical porous yet densely packed nanostructure and a narrow size distribution via a low-cost ultrasound assisted method in the presence of Fe^{2+} ions. The synthesis was carried out at a constant temperature in a range of 25−70 °C under ultrasound irradiation. The addition of Fe^{2+} is crucial to adjust the nucleation and growth rates of MnO_2. Detailed characterizations reveal that single-crystalline Fe_3O_4 particles of 3−5 nm in diameter are homogeneously distributed throughout the spheres but none are on surface, and many upright standing MnO_2 nanoflakes result in rough surfaces. To the best of our knowledge, it is the first time to present such composite structures. The involved Fe^{2+} and ultrasound assisted growth mechanism is discussed in detail. The dependence of Fe_3O_4-

MnO_2 molar ratio, sphere diameter and porosity on reaction parameters including reaction temperature (T) and Fe^{2+} concentration (C_{Fe}^{2+}) is investigated. The electrochemical properties of the composites are discussed by comparing with MnO_2 obtained without Fe^{2+}. The SC is optimized via a systematic variation of reaction parameters.

2. EXPERIMENTAL SECTION

2.1. Synthesis of Fe_3O_4−MnO_2 Composites. $MnSO_4$, $(NH_4)_2S_2O_8$, $FeSO_4$, and ethanol were purchased from Shanghai Chemical Reagent Ltd. All chemicals are of analytical grade purity, and used as received without further purification. Deionized water with a resistivity above 18.0 MΩ cm was from a JL-RO100 Millipore-Q Plus water purifier and used directly. In a typical experiment, 0.68 g of $MnSO_4$ and 0.92 g of $(NH_4)_2S_2O_8$ were dissolved in 40 mL of deionized water, and 10 mL of 1.0 mM $FeSO_4$(aq) was then added. Thus, a mixture containing 0.08 M Mn^{2+} and 0.2 mM Fe^{2+} was obtained. The mixed solution was ultrasonic irradiated for 1.5 h at a power of 100 W in a thermostatic water bath at 50 °C. The resulting precipitates were collected by centrifugation and washed with deionized water and ethanol repeatedly. Finally, the products were freeze-dried for 12 h.

2.2. Characterizations. The products were characterized by X-ray diffraction (XRD) with a D/Max-RA X-ray diffractometer (using Cu Kα = 1.5418 Å radiation) at a scan rate of 1°/min. The morphology and sizes of the products were analyzed by field-emission scanning electron microscopy (FE-SEM, S-4800, Hitachi) at 10 kV and transmission electron microscopy (TEM, JEM-2100, JEOL) at an acceleration voltage of 200 kV. Energy dispersed X-ray spectroscopy (EDS) was performed on the same FE-SEM microscope. To ensure a high accuracy, the atomic percentages from repeated EDS measurements at different positions were averaged. The valence states of elements were examined by X-ray photoelectron spectroscopy (XPS) that was performed in a Thermo VG Scientic MultiLab ESCA2000 system with a CLAM4 hemispherical analyzer and at a base pressure below 3×10^{-10} mbar. Photoelectrons were collected through the hemispherical energy analyzer with pass energy of 20 eV. Since the spherical composites in this study are about 700 nm in diameter, XPS depth profiling can be employed with confidence. Depth profiling was performed using a 3 keV Ar^+ ion beam. XPS data were collected between the sputtering cycles of 100 s. N_2 adsorption isotherms were measured at 77 K on a Micromeritics ASAP2020 instrument. The specific surface areas and the pore-size distributions were determined using the Brunauer−Emmett−Teller (BET) and the Barrett−Joyner−Halenda (BJH) methods, respectively.

2.3. Electrochemical Measurements. As for the preparation of working electrodes, nickel foams were ultrasonicated in 1 M NaOH for 10 min, and then washed with 1 M HCl, ethanol, and deionized water successively. Then a mixture containing 70 wt % Fe_3O_4−MnO_2 composites, 20 wt % acetylene black, and 10 wt % polytetrafluoroethylene binder was pressed with 10 MPa onto the nickel foam. The effective area of a working electrode of Fe_3O_4−MnO_2 is 1 cm^2 and the typical mass loading of electrode material is about 2 mg.

The electrochemical performance of the Fe_3O_4−MnO_2 composites was studied by cyclic voltammetry (CV) and galvanostatically charge−discharge (CD) cycling. The electrochemical measurements were carried out on an Autolab 302N electrochemical workstation in a three-electrode system with a platinum foil counter electrode and an Ag/AgCl reference. The used electrolyte was 1 M Na_2SO_4(aq). CV cans were recorded from 0 to 1.0 V (vs Ag/AgCl) at scan rates of 1, 5, 10, 20, 30, 50, and 100 mV/s. Specific capacitance of the Fe_3O_4−MnO_2 composites was calculated using the following formula $SC = \int i\mathrm{d}V/(2\nu\ m\Delta V)$, where $\int i\mathrm{d}V$ is the integral under the CV curve calculated by the software, ν is the scan rate, m is mass of the active material, and ΔV is the operating potential range. CD cycle tests were carried out in the range of 0−1.0 V at a charge/discharge current density of 5 A/g. Capacitance retention was tested on a battery analyzer (Betta TeQ). The anode is the same as the above-described working electrode, and the cathode is blank nickel foam. They were

assembled by using PE fibrous paper as a separator and 1 M Na_2SO_4(aq) as the electrolyte. The current density and potential windows are the same as those in the CD measurements. The capacitance retention of any cycle equals its discharge time divided by the discharge time of the first cycle.

3. RESULTS AND DISCUSSION

Figure 1a shows a low-magnification SEM image of the products obtained from a typical experiment (C_{Fe}^{2+} = 0.2 mM, T = 50 °C, and t = 1.5 h). The products are isolated, spherical particles with a diameter of (0.7 ± 0.15) μm according to a statistics of 100 particles (Figure 1b). High-magnification SEM (Figure 1c) reveals that they have a hierarchical nanostructure. The surfaces show numerous randomly distributed, interconnecting nanoflakes, resulting in a porous structure with many cavities between adjacent flakes. The SEM-EDS spectrum (Figure 1d) shows only the Mn, O, and Fe characteristic peaks. The relatively weak peak at ~2.2 keV should be assigned to elemental S, which is due to the remnant $(NH_4)_2S_2O_8$. The peak at 6.5 keV is from the overlapping signals of Fe and Mn, as observed in previous reports on Fe−Mn composites.[9,27] Many elements have overlapping peaks (e.g., Ti Kβ and V Kα, Mn Kβ and Fe Kα) because the energy levels for different elements are too close to be distinguishable from each other. The atomic percentages of Fe and Mn are 2.4 at. % and 32.4 at. %, respectively. That is to say, Fe/Mn atomic ratio in the sample is r = 0.075. The result proves that the sample consists of Mn and Fe oxides. The overlapping peak at 6.5 keV is very weak compared with other characteristic peaks of Mn and Fe, thus its influence on accuracy of EDS quantitative analysis is negligible. Figure 1e shows a SEM image of one composite particle and an X-ray elemental mapping recorded from the selected frame. The distribution of the three elements was revealed (on the right). Because Mn (red), Fe (green), and O (cyan) elements are distributed throughout the whole sphere (Figure 1f), the simultaneous presence of Fe (green) and O (cyan) combines into a bright yellowish color (Figure 1e), revealing that the Fe oxides are homogeneously distributed as isolated nanoparticles.

As shown in the XRD pattern (Figure 2) of the typical products, all diffraction peaks are indexed to pure phases of MnO_2 (JCPDS No. 30-0820) and Fe_3O_4 (JCPDS No. 65-3107). The 2θ scan's peaks at 37.12° and 66.75° correspond to the (100) and (110) diffractions of MnO_2, and the peaks at
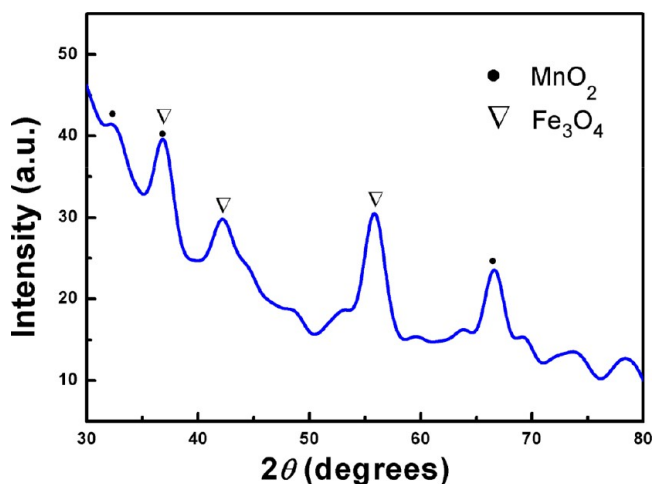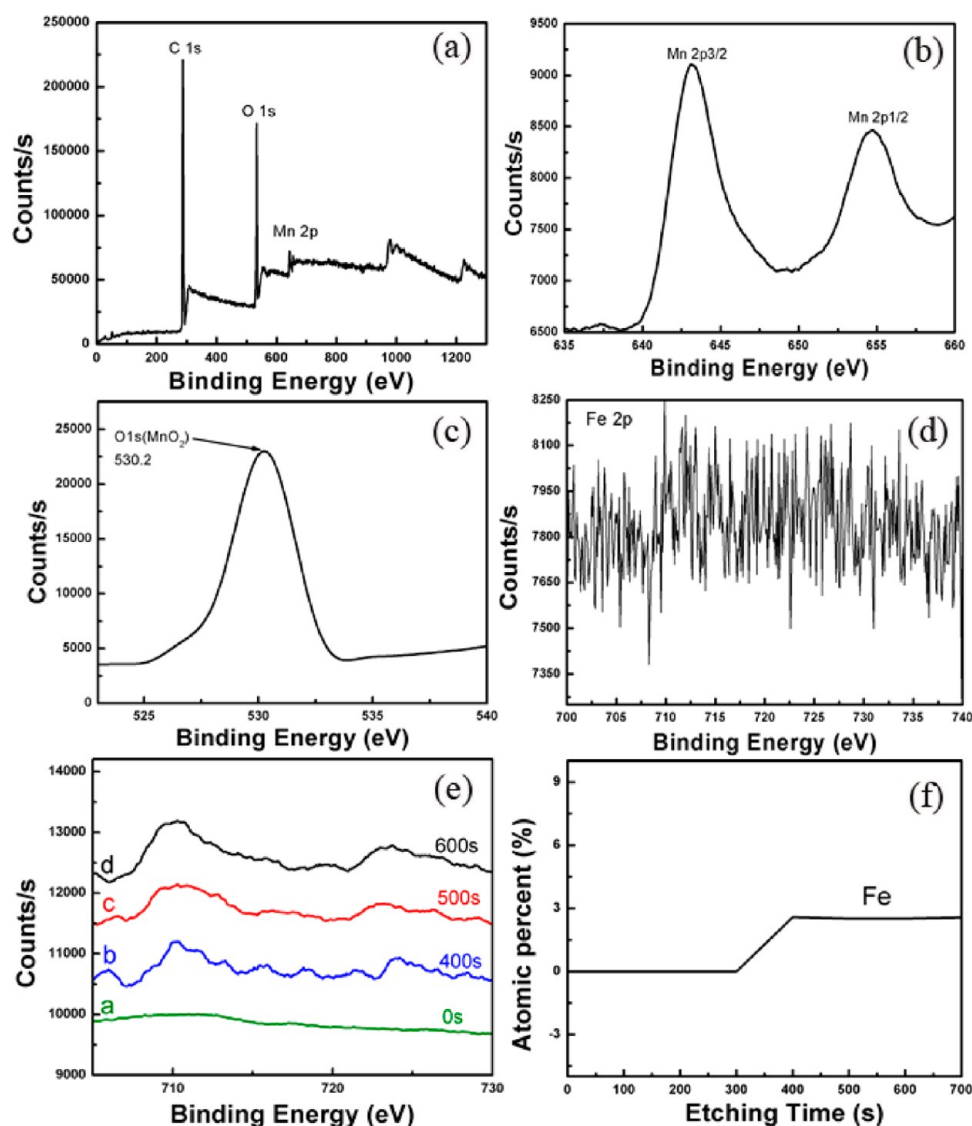

Figure 2. XRD pattern of the typical sample as shown in Figure 1.

17639

dx.doi.org/10.1021/am505622c | *ACS Appl. Mater. Interfaces* 2014, 6, 17637−17646

Figure 3. (a) XPS survey spectrum, and high resolution XPS spectra of (b) Mn 2p, (c) O 1s, and (d) Fe 2p peaks for the typical Fe_3O_4–MnO_2 composite. (e) XPS depth profile of Fe 2p signals from the typical composite spheres, after sputtering for 0, 400, 500, and 600 s, corresponding to curves from a to d, respectively. (f) Change of atomic percentages of Fe in Fe_3O_4–MnO_2 composites with the etching time.

37.09°, 43.09°, and 56.98° correspond to the (222), (400), and (511) diffractions of Fe_3O_4. This further confirms that the composite consists of MnO_2 and Fe_3O_4. The average grain sizes of MnO_2 and Fe_3O_4 in the composite are calculated to be respectively 9 and 5 nm, according to the Scherrer equation $d = 0.9\lambda/\beta_{1/2}\cos\theta$, where d is the average grain size (nm), λ is the wavelength of the used X-ray (0.154 18 nm), and $\beta_{1/2}$ is the width of the diffraction peak at half height. This is consistent with the result from SEM-EDS surface scanning mapping (Figure 1e), and indicates that the Fe_3O_4 nanoparticles inside of a sphere are single crystalline.

The XPS survey (Figure 3a) shows only C, O, and Mn are present in the composite. Note that the appearance of the C 1s peak is attributed to the carbon tape for fixing samples. The spectra have been referenced to the C 1s peak at 284.5 eV. As illustrated in Figure 3b, the binding energies of the Mn $2p_{3/2}$ and $2p_{1/2}$ states are located at 642.0 and 654.8 eV, respectively. This indicates a tetravalent state of Mn in the sample. In high resolution XPS spectrum of the O 1s (Figure 3c), only a strong peak for the elemental O corresponding to pure MnO_2 is

observed at 530.2 eV. An absence of peaks in the high-resolution Fe 2p XPS spectrum (Figure 3d) indicates that no Fe oxides are in the surface layer of the spheres since XPS analysis collects information on several nanometers depth away from the outer surface of samples.

Figure 3e shows the XPS depth profile of the Fe 2p signals after Ar^+ sputtering for various durations up to 800 s. Again, no Fe 2p is discerned before sputtering (green curve a), confirming the absence of Fe_3O_4. Notice that the spectra taken after less than 400 s of sputtering show no an obvious change, and are thus not presented. After 400 s of sputtering, weak Fe 2p peaks occur (blue curve b), indicating that Fe_3O_4 starts to appear there. The peaks' intensity increases with the etching time (curves from b to d), and the two peaks both become even better resolved and smoother after sputtering for 600 s (black curve d). Their observed positions are at binding energies of 711.1 and 724.8 eV, respectively, confirming the Fe to be in Fe_3O_4. That the XPS spectra do not change anymore after etching times above 600 s (the spectra taken after longer than 600 s are not shown) indicates that Fe_3O_4 nanoparticles are

homogeneously distributed in a volume under a surface layer inside of the spheres. In most cases, a porous material etches more rapidly than a solid one due to its inherently lower mass density. The etching rate of porous MnO_2 is several times that of solid MnO_2, which is not known but close to that of solid Fe_3O_4 (7.5 nm/min[28]). Therefore, this procedure provides a depth profile analysis of any other metal oxide objects that are several hundreds of nanometers in diameter (>100 nm). The thickness of the pure MnO_2 layer is at least larger than 50 nm. A systematic comparative study on XPS depth etching of solid and porous MnO_2 needs to be done in the future in order to obtain an accurate size of the MnO_2 layer thickness.

A low-magnification TEM image (Figure 4a) shows that the products have a spherical morphology, and they are quite
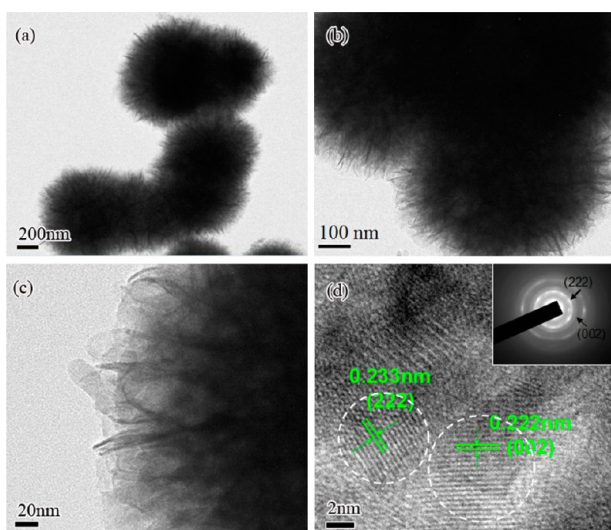
Figure 4. (a−c) TEM images with different magnifications, and (d) HRTEM image of the typical products as shown in Figure 1. The inset shows SAED pattern recorded from a single composite particle.

porous almost throughout, also internally. The spheres' surface looks to be very rough, which is consistent with SEM observations. High-magnification TEM images (Figure 4b,c) recorded from an edge of a sphere display its loose-packed structure made from many nanoflakes that reach far into the interior. The HRTEM image in Figure 4d indicates that the composite has good crystallinity but is not single crystalline (various domains with different crystallographic orientations are marked with dashed circles). The distances between the lattice planes along different directions in different grains are measured to be 0.222 and 0.233 nm, which is in accord with the (002) lattice spacing of MnO_2 and (222) lattice spacing of Fe_3O_4, respectively. Single-crystalline Fe_3O_4 particles have diameters of 3−5 nm, consistent with the XRD results. The selected area diffraction (SAED) pattern (inset of Figure 4d) recorded from one sphere confirms its polycrystalline nature, and the main diffraction rings correspond to MnO_2 and Fe_3O_4.

Figure 5 shows SEM images of products from different reaction temperatures T while other conditions are typical. At room temperature, the products are spherical particles with an average diameter of 0.4 ± 0.10 μm, but the reaction is relatively slow and few products are obtained after 1.5 h. At a higher temperature of 40 °C, isolated, spherical porous structures are obtained, and their diameters increase to 0.54 ± 0.12 μm (Figure 5a). At the typical 50 °C, hierarchically porous particles

with an average diameter of 0.7 ± 0.15 μm are synthesized, as shown in Figure 1. When T is increased to 60 °C (Figure 5b), the products are still hierarchically porous spheres, and the diameter increases to 1.0 ± 0.10 μm. At a higher T of 70 °C, however, well-formed and isolated spheres are no longer attainable, but spherical aggregates with loose-packed structure and larger diameters of 1.28 ± 0.12 μm are obtained instead (Figure 5c). This indicates that the diameters of spherical products highly depend on T. The diameter versus T curve in Figure 5d illustrates how the spheres' diameters increase with T. Interestingly, the diameter increases linearly with T higher than 50 °C. The increase rate of diameter with T is about 2.5 times faster than that at lower temperatures. In addition, the surface morphology of spherical composite particles is influenced by the reaction temperature. When T is increased to 70 °C, the upright standing and intersecting nanosheets on the surfaces disappear.

In the absence of Fe^{2+}, the reaction is much slower, the generation of MnO_2 particles is not noticeable, and even the reaction solution shows no observable color change after half an hour. After the addition of Fe^{2+}, an obvious color change of the reaction solution from colorless to black was observed after about 20 min. Also, a significant increase in sphere diameter from 540 nm ($C_{Fe^{2+}} = 0.1$ mM) to 700 nm ($C_{Fe^{2+}} = 0.2$ mM) further confirms a faster growth of MnO_2 induced by Fe^{2+} (Figure S1b,c, Supporting Information). The gradual increase of Fe atomic percentage is direct evidence for the increasing content of Fe_3O_4 in the composites as $C_{Fe^{2+}}$ increases from 0.1 to 0.3 mM. Semiquantitative EDS analysis determines the Fe/Mn atomic ratios (Figure 6) in the five samples obtained with different $C_{Fe^{2+}}$ of 0.10, 0.16, 0.20, 0.24, and 0.30 mM to be 0.053, 0.068, 0.075, 0.089, and 0.110, respectively. This indicates that composition modulation of the composites can be achieved by $C_{Fe^{2+}}$. Moreover, calculating the theoretical yield expected from the $C_{Mn^{2+}}$ and $C_{Fe^{2+}}$ values and the stoichiometry of the oxidation reactions confirms these ratios once more, and thus proves that the reactions came to completion in the allowed 1.5 h reaction time.

On the basis of the above observations, the growth mechanism of hierarchically porous MnO_2−Fe_3O_4 structures is suggested as follows (see Scheme 1). Fe^{2+} and Mn^{2+} in the mixed solution are oxidized simultaneously by $(NH_4)_2S_2O_8$. The Fe^{2+} not only works for providing Fe element but also acts as a catalyst for the Mn^{2+} oxidation and thus adjusts the nucleation and growth rates of MnO_2. Under continuous ultrasonic irradiation, the presence of Fe^{2+} makes a solution containing high concentrations of MnO_2 and Fe_3O_4, which ensures a rapid nucleation. As a result, there is rapid nucleation but relatively slow growth, so that a large quantity of MnO_2 and Fe_3O_4 nuclei combine to form small crystallites. Due to minimization of surface energy, these crystallites aggregate into spherical shapes. The number density per unit volume of Fe_3O_4 crystallites is much lower than that of MnO_2 due to the low $C_{Fe^{2+}}$. The Fe_3O_4 crystallites are circled by MnO_2 and thus embed during the formation of spherical particles. These steps are not rapid without Fe^{2+} being present, and the absence of Fe^{2+} leads to MnO_2 with irregular shapes. The ultrasound technique is also crucial for the formation of the desired product. A control experiment in the absence of ultrasonic irradiation shows that no reaction happens after 12 h. Mechanical (magnetic) stirring instead of the ultrasound leads to no obvious color change of reaction solution after 12 h. This crucial influence on the growth mechanism has been
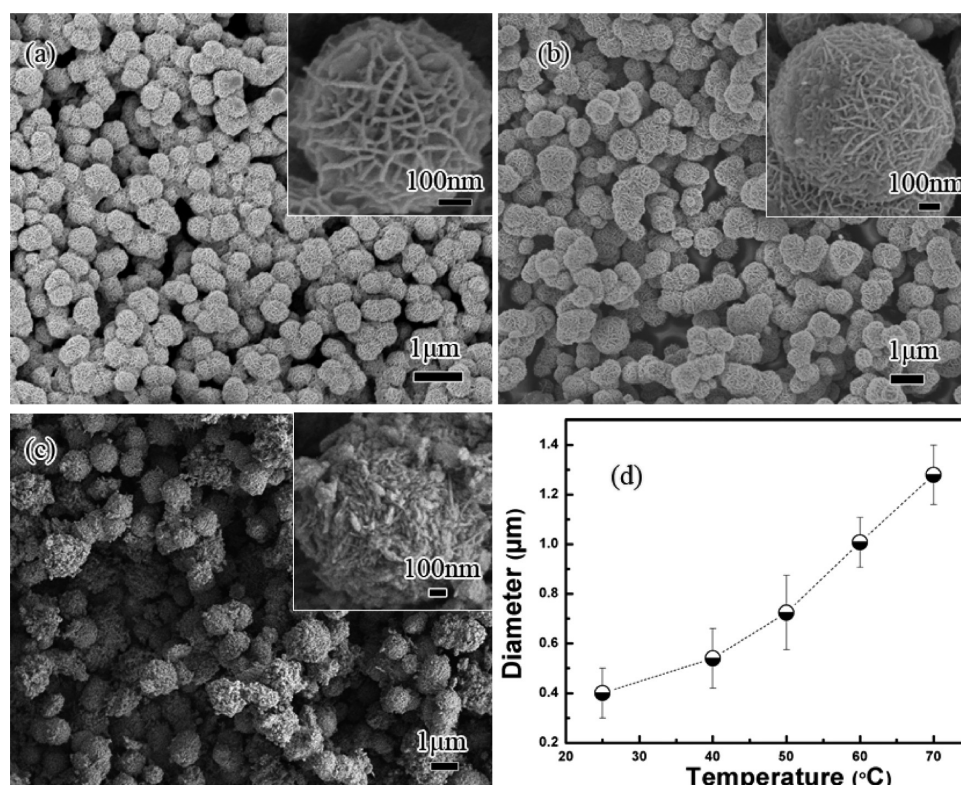
Figure 5. SEM images of products obtained with different reaction temperatures T of (a) 40, (b) 60, and (c) 70 °C while other conditions remained typical. (d) Average particle diameters versus the reaction temperature T.
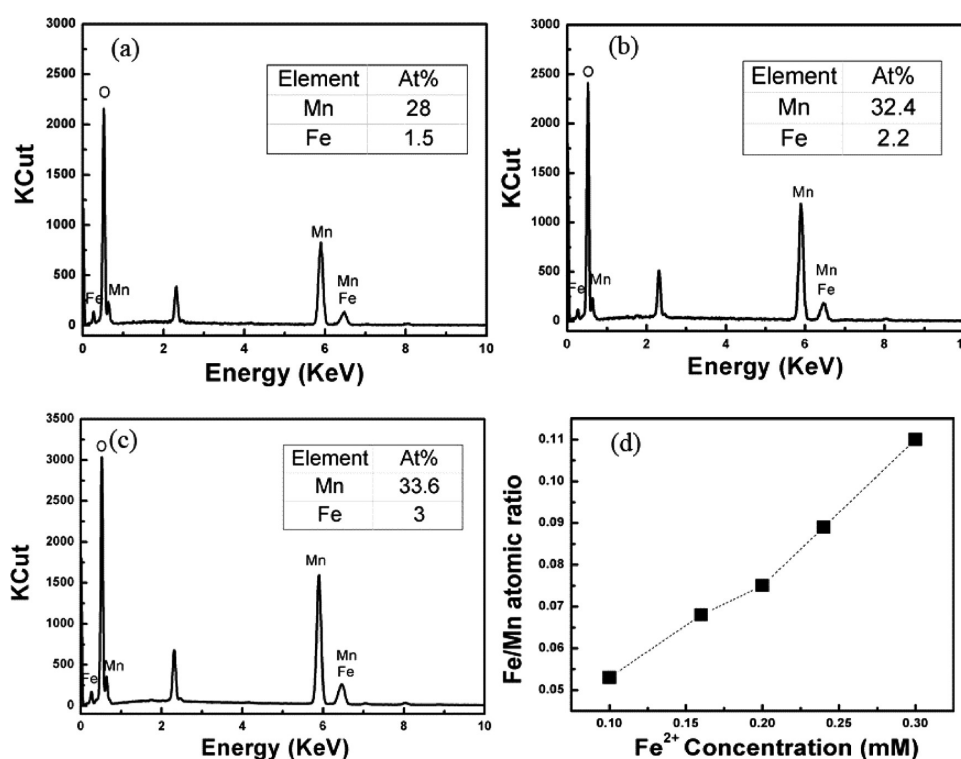
Figure 6. SEM-EDS spectra of the products obtained with different C_{Fe}^{2+} of (a) 0.1 mM, (b) 0.16 mM and (c) 0.24 mM while other conditions remained typical, and (d) Fe/Mn atomic ratios versus C_{Fe}^{2+}.

seen previously in the synthesis of spherical, porous Pd nanostructures.[29] Besides breaking up of local aggregation to avoid the generation of larger aggregates, the ultrasound improves transport of crystallites in the solution and provides a

homogeneous environment,[30] leading to porous spheres rather than allowing the growth of flakes first.

After the aggregation process, all Fe_3O_4 crystallites are used up while some Mn^{2+} ions still remain. With a gradual decrease

**Scheme 1. Illustration of the Growth Process of Fe$_3$O$_4$–MnO$_2$ Composites**
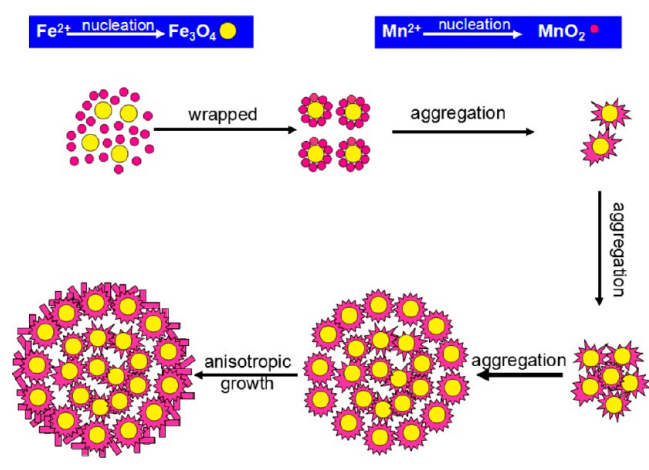
of Mn^{2+} concentration, formation of crystallites and the growth into new spheres stop. According to the constitutional supercooling theory, the remnant Mn^{2+} would not aggregate into new spheres but add to the already present particles. An anisotropic growth builds nanoflakes on the surfaces. Since the Fe^{2+} is used up, no Fe$_3$O$_4$ but only MnO$_2$ flakes stay in the outer layer of the spheres. This is the reason being responsible for the absence of elemental Fe in the surface layer. The analysis of samples taken at different times during the reaction verifies this picture.

It is noted that the role of Fe^{2+} is not only simply providing Fe^{2+} for the complex structure, increasing oxidation rate of Mn^{2+} but also plays an important role in the anisotropic growth of MnO$_2$. In the absence of Fe^{2+}, the reaction is much slower, and not porous spheres but MnO$_2$ nanostructures with loose-packed rather irregular shapes resulted (Figure S1a, Supporting Information), whereas adding Fe^{2+} always obtains hierarchically porous microspheres. A control experiment using Fe^{3+} instead of Fe^{2+} results in aggregates with irregular shapes and sizes (Figure S2, Supporting Information). This may be because the reducibility of Fe^{2+} facilitates an oriented growth. Increasing Mn^{2+} concentration or/and temperature in order to improve the reaction speed does not obtain hierarchical porous structures. Therefore, the presence of catalytic Fe^{2+} is crucial, but the $C_{Fe}{}^{2+}$ must be low to ensure the formation of desired structures. The microspheres are most isolated from each other with a low $C_{Fe}{}^{2+}$ (Figure S1b, Supporting Information), whereas a relatively high $C_{Fe}{}^{2+}$ leads to aggregates of conjoined microspheres with an average diameter of 2 μm, as shown in Figure S1d (Supporting Information).

Figure 7a shows CV curves of the typical Fe$_3$O$_4$–MnO$_2$ composites in Na$_2$SO$_4$ solution at various scan rates. The rectangularity of the curves reveals that the electrochemical capacitances are mainly associated with Faradaic pseudocapacitance.[31] The area of the CV curve increases with the scan rate. The fast and reversible successive surface redox reactions of MnO$_2$ are processed by intercalation/deintercalation processes of the protons according to the reaction 1. The pseudocapacitance reaction of Fe$_3$O$_4$ may result from the redox reactions
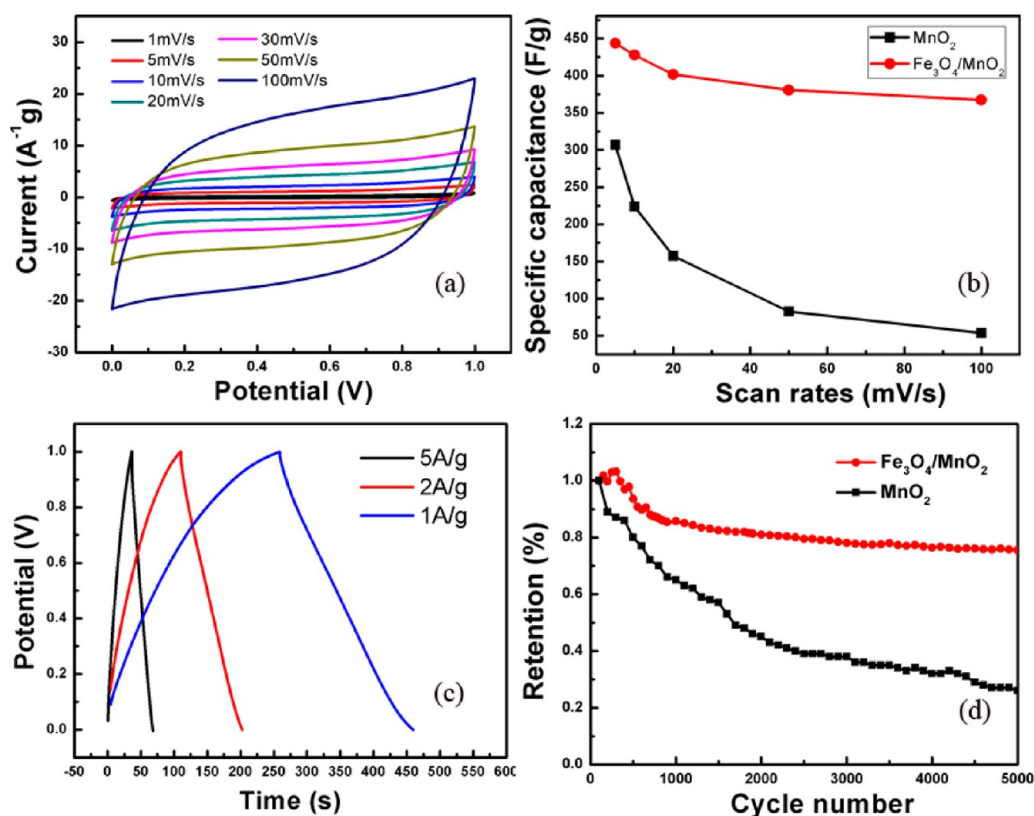
Figure 7. (a) CV curves of the electrode coated with the Fe$_3$O$_4$–MnO$_2$ composites as shown in Figure 1 at various scan rates of 1, 5, 10, 20, 30, 50, and 100 mV/s. (b) SC values of the Fe$_3$O$_4$–MnO$_2$ and the irregular MnO$_2$ versus scan rates. (c) Charge−discharge cycling curves in the potential range from 0 to 1 V in 1 M Na$_2$SO$_4$ at different current densities. (d) Capacitance retention at 5 A/g over 5000 cycles.

between Fe^{2+} and Fe^{3+} accompanied by intercalation of sulfate ions balance the extra charge with the iron oxide layers (2).

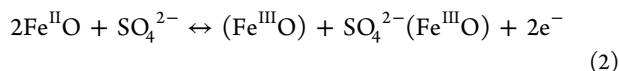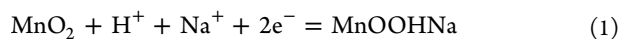$$MnO_2 + H^+ + Na^+ + 2e^- = MnOOHNa \qquad (1)$$

$$2Fe^{II}O + SO_4^{2-} \leftrightarrow (Fe^{III}O) + SO_4^{2-}(Fe^{III}O) + 2e^- \qquad (2)$$

Figure 7b shows the corresponding SC values of the Fe_3O_4−MnO_2 at various scan rates from 1 to 100 mV/s. The SC values of Fe_3O_4−MnO_2 are much higher than those of the irregular MnO_2 nanostructures at the same scan rates. The SC of the Fe_3O_4−MnO_2 is 447.8 F/g at a scan rate of 5 mV/s, which is nearly 1.5 times that of the MnO_2 obtained without Fe^{2+} (306.9 F/g, 5 mV/s) and the extremely high reported value for pure MnO_2 supercapacitive materials (309 F/g, 5 mV/s).[32] At a low a scan rate of 1 mV/s, the SC value of the Fe_3O_4−MnO_2 is up to 536.7 F/g. The high SC is partly attributed to the porosity and a synergistic effect between MnO_2 and Fe_3O_4. The high porosity leads to a higher specific surface area of Fe_3O_4−MnO_2 (83 m²/g) compared to the irregular MnO_2 nanostructures (36 m²/g). Our Fe_3O_4−MnO_2 still has a SC of 367.4 F/g even at 100 mV/s (82.8% of the SC at 5 mV/s), making it a very promising material for high charge/discharge applications. Figure 7c shows the CD characteristics of the Fe_3O_4−MnO_2 composite electrode in a potential range of 0−1.0 V at various specific current densities. The curves indicate that the material has a reversible capacitance of charge/discharge. At a current density of 5 A/g, the discharge time of Fe_3O_4−MnO_2 (32.3 s) is 2 times that of the irregular MnO_2 (16.0 s), meaning that the SC of Fe_3O_4−MnO_2 is about 2 times that of MnO_2, consistent with the CV tests. The capacitance of MnO_2 electrode materials is improved after an incorporation of Fe_3O_4 nanoparticles. The superior performances are due to its high specific surface area and hierarchical architecture, which facilitates electron and ion transport. Also, a synergistic effect between different components of MnO_2 and Fe_3O_4 plays a key role.

The long-term cycle ability of the Fe_3O_4−MnO_2 electrode was evaluated by repeating the CD test. Figure 7d shows the capacitance retention of Fe_3O_4−MnO_2 for 5000 cycles at a current density of 5 A/g, and the irregular MnO_2 obtained without Fe^{2+} is also presented for comparison. The capacitance of irregular MnO_2 decreases monotonously, while the SC of Fe_3O_4−MnO_2 stays surprisingly stable, decreasing slowly to 76% of the initial SC at the completion of 5000 cycles. This is attributed to the unique hierarchical structure, particularly stable composite nanostructure of the Fe_3O_4−MnO_2 with a high-number-density but isolated Fe_3O_4 nanoparticles in the interior of MnO_2. These Fe_3O_4−MnO_2 composite electrodes exhibit much better electrochemical characteristics, demonstrating their potential applications in high-performance supercapacitors.

Figure 8 shows Nyquist plots of the Fe_3O_4−MnO_2 composite and irregular MnO_2 electrodes, which were measured in a frequency range of 100 kHz to 0.1 Hz with an amplitude of 5 mV. The corresponding equivalent circuit (inset) consists of a series and parallel combination of resistances, R_e (contributions of ionic resistance of electrolyte, intrinsic resistance, and contact resistance between active material and current collector), R_{ct} (charge transfer resistance), CPE (constant phase element), and W (Warburg impedance). The semicircle corresponds to a parallel combination of charge-transfer resistance (R_{ct}) and double-layer capacitance.[33] Through a fitting analysis, the related R_{ct} of the Fe_3O_4−
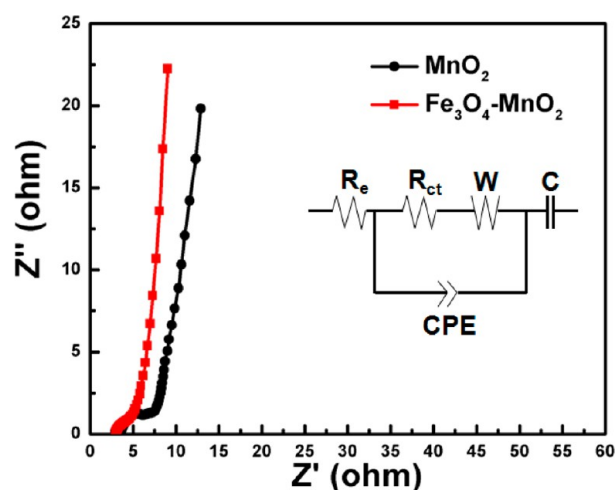
Figure 8. Nyquist plots of Fe_3O_4−MnO_2 composite and irregular MnO_2 electrodes. The inset shows the corresponding equivalent circuit.

MnO_2 composite electrode has a low value of 2.6 Ω, which is even lower than half of the irregular MnO_2 electrode (5.7 Ω). The R_e of the Fe_3O_4−MnO_2 electrode is 1.9 Ω, which is determined by the point where the semicircle intersects with the Z′-axis, also lower than that of the irregular MnO_2 electrode (2.3 Ω). The low values of R_{ct} and R_e are mainly attributed to the high specific surface area of porous Fe_3O_4−MnO_2, which facilitates a charge transfer and a faster ion insertion/extraction during electrochemical reactions. The almost vertical line in the low frequency region is indicative of the rapid ion transport that the porosity allows between electrode and electrolyte as well as through the latter.[34]

An addition of Fe^{2+} always obtains hierarchically porous microspheres and at the same time Fe/Mn atomic ratios are adjustable, which allow us to investigate the synergistic effect between MnO_2 and Fe_3O_4 on the supercapacitive performance. Figure 9 shows a curve of the SC values of the Fe_3O_4−MnO_2 products versus Fe/Mn atomic ratios. At the same scan rate of 5 mV/s, SC values of the Fe_3O_4−MnO_2 with different Fe/Mn atomic ratios of 0, 0.053, 0.068, 0.075, 0.089, and 0.110 are
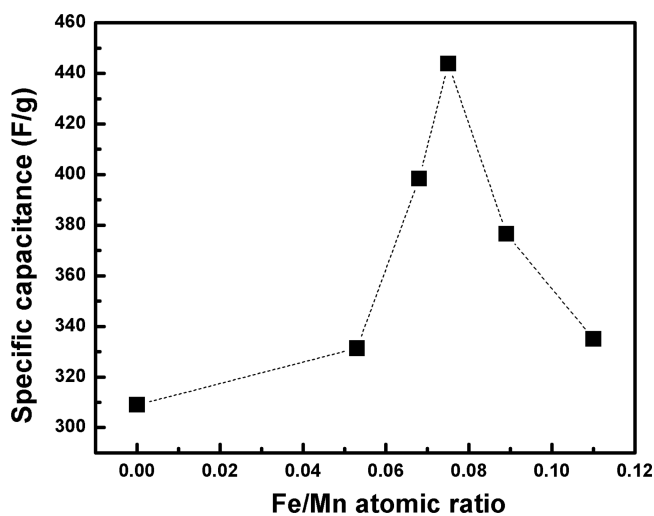
Figure 9. Plot of the specific capacitances of the products versus Fe/Mn atomic ratios.

331.4, 398.4, 447.8, 376.6, and 335.1 F/g, respectively. The SC is optimized to be the highest at an Fe/Mn atomic ratio of 0.075. It is very interesting that very low atomic percentages of Fe in the composites significantly improve the supercapacitive performance. This should be mainly due to the synergistic effect (as discussed later), and partly due to the embedding of Fe_3O_4 nanoparticles by MnO_2 and their homogeneous distribution in the composites. Such nanostructure provides a large quantity of Fe_3O_4/MnO_2 interfaces, and the confinement effects inside the MnO_2 matrix may also enhance electrochemical performance of nanosized Fe_3O_4.[35]

It is well-known that the pseudocapacitive reaction is a surface reaction. Our $MnO_2-Fe_3O_4$ composites are internally porous with a hierarchical structure. The high porosity leads to a specific surface area of 83 m^2/g, much higher than the value (1.7 m^2/g) calculated with the spheres' average diameter (0.7 μm) and the density of MnO_2 (5.0 g/cm^3). Because these internal pores are highly ion-accessible from the outside, the Fe_3O_4 inside participates in the pseudocapacitive reaction. Although the morphology and structure of composites have a respective impact on improving specific capacitance,[36] the composition plays a more significant role. The synergy between MnO_2 and Fe_3O_4 is suggested as follows: (i) Both MnO_2 and Fe_3O_4 are positive pseudocapacitance materials, and can contribute their capacitance. The synergistic effect improves the capacitance of the composites higher than that of individual components alone, similar to that of $Ni(OH)_2-MnO_2$ hybrids.[37,38] (ii) The morphology-dependent specific surface area of the composite spheres does not change with Fe^{2+} concentration, while their SC changes obviously. In many reports on MnO_2 electrode materials,[32,36,39] the specific capacitances are low even if they have a hollow or porous structure allowing a high specific surface area. (iii) The SC does not increase monotonously, but is optimized to be the highest at an Fe/Mn atomic ratio of 0.075. This indicates that the pseudocapacitive performances of the composites are highly composition-dependent, and is also a reflection about the synergistic effect.

The composites here provide a unique structure that should be further investigated and extended in future work. For example, the procedure can embed Fe_3O_4 nanoparticles within spherical porous MnO_2 spheres while retaining the sphere surface for yet further loading with still other materials to form quite complex layered structures. Such layered structures integrate various metal oxides into a single system. Especially, regarding the availability of complexly layered structures, their likely other interesting functions, and the still not optimized, yet already superior electrochemical properties, exploring the properties of the many different composite particles possible should inspire a lot of future research.

4. CONCLUSIONS

In summary, we demonstrate a one-step and low-cost ultrasound assisted method to fabricate hierarchically porous yet densely packed MnO_2 microspheres doped with Fe_3O_4 nanoparticles. Single-crystalline Fe_3O_4 nanoparticles are homogeneously distributed throughout the spheres and none are on the surface. The spheres' average diameter is highly dependent on the temperature, and thus is controllable in a wide range. Optimizing reaction parameters results in isolated, porous, and uniform $Fe_3O_4-MnO_2$ composite spheres with a superior specific capacitance of 448 F/g at a scan rate of 5 mV/s, which is nearly 1.5 times that of the extremely high reported value for pure MnO_2. Also, the composite has excellent cycling performance with a capacitance retention of about 76% after 5000 charge/discharge cycles at 5 A/g. Especially, such a structure allows significantly improves the stability at high charging rates. The $Fe_3O_4-MnO_2$ still has SC of 367.4 F/g even at 100 mV/s, which is 82% of that at 5 mV/s. This makes the novel material very promising in future applications for fast charging applications and also where charging times may vary significantly while the capacitance should stay constant.

■ ASSOCIATED CONTENT

ⓢ Supporting Information

SEM images of the $Fe_3O_4-MnO_2$ composites obtained with different $C_{Fe}{}^{2+}$ while other conditions remained. SEM images of the products using Fe^{3+} instead of Fe^{2+}. This material is available free of charge via the Internet at http://pubs.acs.org.

■ AUTHOR INFORMATION

Corresponding Authors
*S. Tang. Fax: (+86)-25-83595535. E-mail: tangsc@nju.edu.cn.
*X. Meng. Fax: (+86)-25-83595535 E-mail: mengxk@nju.edu. cn.

Author Contributions
‡Jian Zhu and Shaochun Tang contributed equally to this work.

Notes
The authors declare no competing financial interest.

■ REFERENCES

(1) Liu, J.; Xue, D. Thermal Oxidation Strategy towards Porous Metal Oxide Hollow Architectures. *Adv. Mater.* **2008**, *20*, 2622−2627.

(2) Olivares-Marín, M.; Fernández, J. A.; Lázaro, M.; Fernández-González, C.; Macías-García, A.; Gómez-Serrano, V.; Stoeckli, F.; Centeno, T. A. Cherry Stones as Precursor of Activated Carbons for Supercapacitors. *Mater. Chem. Phys.* **2009**, *114*, 323−327.

(3) Lee, M. T.; Chang, J. K.; Hsieh, Y. T.; Tsai, W. T. Annealed Mn-Fe Binary Oxides for Supercapacitor Applications. *J. Power Sources* **2008**, *185*, 1550−1556.

(4) Lu, T.; Zhang, Y. P.; Li, H. B.; Pan, L. K.; Li, Y. L.; Sun, Z. Electrochemical Behaviors of Graphene-ZnO and Graphene-SnO₂ Composite Films for Supercapacitors. *Electrochim. Acta* **2010**, *55*, 4170−4173.

(5) Prasad, K. R.; Miura, N. Electrochemically Synthesized MnO₂-based Mixed Oxides for High Performance Redox Supercapacitors. *Electrochem. Commun.* **2004**, *6*, 1004−1008.

(6) Qian, W.; Chen, Z. Q.; Cottingham, S.; Merrill, W. A. Surfactant-Free Hybridization of Transition Metal Oxide Nanoparticles with Conductive Graphene for High-Performance Supercapacitor. *Green Chem.* **2012**, *14*, 371−377.

(7) Tang, S. C.; Vongehr, S.; Wang, Y. G.; Cui, J.; Wang, X. Y.; Meng, X. K. Versatile Synthesis of High Surface Area Multi-Metallic Nanosponges Allowing Control over Nanostructure and Alloying for Catalysis and SERS Detection. *J. Mater. Chem. A* **2014**, *2*, 3648−3660.

(8) Yu, W.; Jiang, X. B.; Ding, S. J.; Li, B. Q. Preparation and Electrochemical Characteristics of Porous Hollow Spheres of NiO Nanosheets as Electrodes of Supercapacitors. *J. Power Sources* **2014**, *256*, 440−448.

(9) Dubal, D. P.; Kim, W. B.; Lokhande, C. D. Galvanostatically Deposited Fe: MnO_2 Electrodes for Supercapacitor Application. *J. Phys. Chem. Solids* **2012**, *73*, 18−24.

(10) Wang, G. X.; Tang, Q. Q.; Bao, H.; Li, X. W.; Wang, G. C. Synthesis of Hierarchical Sulfonated Graphene/MnO_2/Polyaniline Ternary Composite and its Improved Electrochemical Performance. *J. Power Sources* **2013**, *241*, 231−238.

(11) Zhang, B. J.; Li, W. Y.; Sun, J. Q.; He, J. G.; Zou, R. J.; Hu, J. Q.; Chen, Z. G. NiO/MnO_2 Core/Shell Nanocomposites for High-Performance Pseudocapacitors. *Mater. Lett.* **2014**, *114*, 40−43.

(12) Zhang, Y. X.; Li, F.; Huang, M. One-Step Hydrothermal Synthesis of Hierarchical MnO_2-Coated CuO Flower-like Nanostructures with Enhanced Electrochemical Properties for Supercapacitor. *Mater. Lett.* **2013**, *112*, 203−206.

(13) Sarkar, D.; Khan, G. G.; Singh, A. K.; Mandal, K. High-Performance Pseudocapacitor Electrodes Based on α-Fe_2O_3/MnO_2 Core−Shell Nanowire Heterostructure Arrays. *J. Phys. Chem. C* **2013**, *117*, 15523−15531.

(14) Dhibar, S.; Das, C. K. Silver Nanoparticles Decorated Polyaniline/Multiwalled Carbon Nanotubes Nanocomposite for High-Performance Supercapacitor Electrode. *Ind. Eng. Chem. Res.* **2014**, *53*, 3495−3508.

(15) Pusawale, S. N.; Deshmukh, P. R.; Lokhande, C. D. Chemical Synthesis of Nanocrystalline SnO_2 Thin Films for Supercapacitor Application. *Appl. Surf. Sci.* **2011**, *257*, 9498−9502.

(16) Liu, Y.; Jiao, Y.; Zhang, Z. L. Hierarchical SnO_2 Nanostructures Made of Intermingled Ultrathin Nanosheets for Environmental Remediation, Smart Gas Sensor, and Supercapacitor Applications. *ACS Appl. Mater. Interfaces* **2014**, *6*, 2174−2184.

(17) Wang, L.; Ji, H. M.; Wang, S. S. Preparation of Fe_3O_4 with High Specific Surface Area and Improved Capacitance as a Supercapacitor. *Nanoscale* **2013**, *5*, 3793−3799.

(18) Wang, L.; Zhang, X. X.; Wang, S. S. Ultrasonic-Assisted Synthesis of Amorphous Fe_3O_4 with a High Specific Surface Area and Improved Capacitance for Supercapacitor. *Powder Technol.* **2014**, *256*, 499−505.

(19) Wang, Q. H.; Jiao, L. F.; Du, H. M. Fe_3O_4 Nanoparticles Grown on Graphene as Advanced Electrode Materials for Supercapacitors. *J. Power Sources* **2014**, *245*, 101−106.

(20) Wang, B. B.; Fu, X. X.; Shi, S. L.; Cheng, J. P.; Zhang, X. B. Fabrication and Gas Sensing Properties of Hollow Core-Shell SnO_2/α-Fe_2O_3 Heterogeneous Structures. *J. Alloys Compd.* **2014**, *587*, 82−89.

(21) Li, P. X.; Yang, Y. B.; Shi, E. Z. Core-Double-Shell, Carbon Nanotube@Polypyrrole@MnO_2 Sponge as Freestanding, Compressible Supercapacitor Electrode. *ACS Appl. Mater. Interfaces* **2014**, *6*, 5228−5234.

(22) Nam, K. W.; Ma, S. B.; Yoon, W. S. Novel Concept of Pseudocapacitor Using Stabilized Lithium Metal Powder and Non-Lithiated Metal Oxide Electrodes in Organic Electrolyte. *Electrochem. Commun.* **2009**, *11*, 1166−1169.

(23) Jiang, J.; Kucernak, A. Electrochemical Supercapacitor Material Based on Manganese Oxide: Preparation and Characterization. *Electrochim. Acta* **2002**, *47*, 2381−2386.

(24) Dai, Y. M.; Tang, S. C.; Vongehr, S.; Meng, X. K. Silver Nanoparticle-Induced Growth of Nanowire-Covered Porous MnO_2 Spheres with Superior Supercapacitance. *ACS Sustainable Chem. Eng.* **2014**, *2*, 692−698.

(25) Dong, Q.; Wang, G.; Hu, H.; Yang, J.; Qian, B. Q.; Ling, Z.; Qiu, J. S. Ultrasound-Assisted Preparation of Electrospun Carbon Nanofiber/Graphene Composite Electrode for Supercapacitors. *J. Power Sources* **2013**, *243*, 350−353.

(26) Pendashteh, A.; Rahmanifar, M. S.; Mousavi, M. F. Morphologically Controlled Preparation of CuO Nanostructures under Ultrasound Irradiation and Their Evaluation as Pseudocapacitor Materials. *Ultrason. Sonochem.* **2014**, *21*, 643−652.

(27) Pillis, M. F.; Correa, O. V. Oxidation Behavior of FeCr and FeCrY Alloys Coated with an Aluminium based Paint. *Mater. Res.* **2008**, *11*, 251−256.

(28) Steinberger, R.; Duchoslav, J.; Arndt, M.; Stifter, D. X-ray Photoelectron Spectroscopy of the Effects of Ar^+ Ion Sputtering on the Nature of Some Standard Compounds of Zn, Cr, and Fe. *Corros. Sci.* **2014**, *82*, 154−164.

(29) Tang, S. C.; Vongehr, S.; Zheng, Z.; Ren, H.; Meng, X. K. Facile and Rapid Synthesis of Spherical Porous Palladium Nanostructures with High Catalytic Activity for Formic Acid Electro-Oxidation. *Nanotechnology* **2012**, *23*, 255606.

(30) Tang, S. C.; Meng, X. K.; Lu, H. B. PVP-Assisted Sonoelectrochemical Growth of Silver Nanostructures with Various Shapes. *Mater. Chem. Phys.* **2009**, *116*, 464−468.

(31) Chen, C. C.; Tsay, C. Y.; Lin, H. S.; Jheng, W. D.; Lin, C. K. Effect of Iron Particle Addition on the Pseudocapacitive Performance of Sol-Gel Derived Manganese Oxides Film. *Mater. Chem. Phys.* **2012**, *137*, 503−510.

(32) Yu, C. C.; Zhang, L. X.; Shi, L. A Simple Template-Free Strategy to Synthesize Nanoporous Manganese and Nickel Oxides with Narrow Pore Size Distribution, and Their Electrochemical Properties. *Adv. Funct. Mater.* **2008**, *18*, 1544−1554.

(33) Wei, W. F.; Cui, X. W.; Chen, W. X.; Ivey, D. G. Electrochemical Cyclability Mechanism of MnO_2 Electrodes Utilized as Electrochemical Supercapacitors. *J. Phys. Chem. C* **2008**, *112*, 15075−15083.

(34) Wan, L.; Xiao, J. W.; Xiao, F.; Wang, S. Nanostructured (Co, Ni)-based Compounds Coated on a Highly Conductive Three Dimensional Hollow Carbon Nanorod Array (HCNA) Scaffold for High Performance Pseudocapacitors. *ACS Appl. Mater. Interfaces* **2014**, *6*, 7735−7742.

(35) Wang, Q. G.; Jiao, L. F.; Du, H. M.; Wang, Y. J.; Yuan, H. T. Fe_3O_4 Nanoparticles Grown on Graphene as Advanced Electrode Materials for Supercapacitors. *J. Power Sources* **2014**, *245*, 101−106.

(36) Zhang, X.; Sun, X. Z.; Zhang, H. T.; Zhang, D. C.; Ma, Y. W. Microwave-Assisted Reflux Rapid Synthesis of MnO_2 Nanostructures and Their Application in Supercapacitors. *Electrochim. Acta* **2013**, *87*, 637−644.

(37) Chen, H.; Hu, L.; Yan, Y.; Chen, R.; Chen, M.; Wu, L. One-Step Fabrication of Ultrathin Porous Nickel Hydroxide-Manganese Dioxide Hybrid Nanosheets for Supercapacitor Electrodes with Excellent Capacitive Performance. *Adv. Energy Mater.* **2013**, *3*, 1636−1646.

(38) Chen, H.; Zhou, S. X.; Wu, L. M. Porous Nickel Hydroxide-Manganese Dioxide-Reduced Graphene Oxide Ternary Hybrid Spheres as Excellent Supercapacitor Electrode Materials. *ACS Appl. Mater. Interfaces* **2014**, *6*, 8621−8630.

(39) Munaiah, Y.; Gnana Sundara Raj, B.; Prem Kumar, T.; Ragupathy, P. Facile Synthesis of Hollow Sphere Amorphous MnO_2: The Formation Mechanism, Morphology and Effect of a Bivalent Cation-Containing Electrolyte on Its Supercapacitive Behavior. *J. Mater. Chem. A* **2013**, *1*, 4300−4306.

17646

dx.doi.org/10.1021/am505622c | *ACS Appl. Mater. Interfaces* 2014, 6, 17637−17646